Development of Bipolar-charged Electret Rotatory Power Generator and Application in Self-powered Intelligent Thrust Bearing

Kai Tao[a*], Zhe Zhao[a], Yang Yang[a,b], Jin Wu[c*], Li Yunjia[d], Fan Kangqi[e], Yongqing Fu[f], Honglong Chang[a], Weizheng Yuan[a*]

[a]Ministry of Education Key Laboratory of Micro and Nano Systems for Aerospace, Northwestern Polytechnical University, Xi'an 710072, PR China

[b]Research & Development Institute in Shenzhen, Northwestern Polytechnical University, Shenzhen, 518057, PR China

[c]State Key Laboratory of Optoelectronic Materials and Technologies, Key Laboratory of Display Material and Technology, School of Electronics and Information Technology, Sun Yat-sen University, Guangzhou 510275, PR China

[d]School of Electrical Engineering, Xi'an Jiaotong University, Xi'an 710049, PR China

[e]School of Mechano-Electronic Engineering, Xidian University, Xi'an 710071, PR China

[f]Faculty of Engineering and Environment, Northumbria University, Newcastle upon Tyne, NE1 8ST, UK.

Submitted to: Nano Energy

Corresponding authors:
taokai@nwpu.edu.cn; wujin8@mail.sysu.edu.cn; yuanwz@nwpu.edu.cn

ABSTRACT

Inspired by an electromagnetic hydropower station that contains a reverse polarized magnet, we proposed a new design methodology of electret rotatory energy harvester (e-REH) with bipolar-charged electrets for boosting its output performance. A selectively localized corona discharging method is invented to have both positive and negative ultra-high-resolution charges implanted into a single electret thin film. A generalized theoretical model of bipolar-charged e-REHs with free-standing (Fe-REH) and sliding (Se-REH) operation modes is derived to evaluate their performance. The key features affecting their performance are the initial and parasitic capacitances with different connection schemes. Experimental results show that: the output power of the bipolar-charged e-REH is increased to 392.2% compared to those of the positive alone and negative alone configurations, which fully agree with those obtained from the theoretical model. For the first time, an intelligent thrust ball bearing is designed and fabricated with its self-powered and self-sensing capabilities based on the bipolar-charged e-REH. The rotation speed of the bearing is characterized by the response frequencies of the output voltage by Fast Fourier Transform instead of the output voltage amplitudes, exhibiting an ultra-high frequency sensitivity of 15.0 rpm/Hz and a good linearity R^2 (coefficient of determination) of 99.9%. The developed e-REH has potential applications for high-precision and self-powered intelligent rotation-speed sensing.

KEYWORDS

Electret power generator; Energy harvesting; Intelligent thrust bearing; Bipolar electrets; Self-powered sensing

1. INTRODUCTION

With the rapid development of Internet of Things, wearable devices, and big data technology, energy harvesting from natural resources or human motions has attracted extensive attention as a potential and sustainable energy source [1-6]. So far there are five main mechanisms of harvesting mechanical energy from the ambient environment, e.g., electrostatic [7-9], electromagnetic [10-14], piezoelectric [15-20], triboelectric [21-27] and magnestrictive mechanisms [28]. Among them, triboelectric nanogenerators (TENGs) based on coupling of triboelectric effect and electrostatic induction have exhibited obvious advantages such as low cost [29], versatile choices of materials and structures [30], light weight [31], and high energy conversion efficiency under low-frequency motions [32]. The TENGs are widely applied to harvest energy from wind [33, 34], water [35-38], mechanical vibration [39,40] and human movement [41-45]. They have been developed with a variety of structures and different operation modes, including contact-separation mode [46], sliding mode [47,48], single-electrode mode [49] and freestanding mode [50,51].

As a kind of electrostatic generator developed from TENGs, electret generators not only inherit most advantages of TENGs but also possess extra merits due to their non-contact rotating nature, such as no problems of friction and wear, long service life, high output, and good performance [52-54]. Recently, numerous approaches have been developed to improve the performance of electret-based TENGs, including increasing the effective charge density, applying innovative structures [55-57], and controlling the operating environment [58-60]. Among these, one effective method is to increase the surface charge density of electret material, through applying material selection methodology [61,62], etched and micro/nano-structured surfaces [63], charge pumping technique [64] and chemical surface modification [65]. For electret-based rotary power generators (e-REHs), their effective charge density can be doubled by applying patterned bipolar polarization of electret thin films, which is the integration of both positively and negatively charged electrets into a single rotational energy conversion system [66,67]. However, the polarization process based on the conventional corona charging has critical issues of uneven charging and inability to achieve precise

micro-nano patterned charge injection. On the other hand, various e-REHs with non-contact sliding mode (Se-REH) and freestanding mode (Fe-REH) have been reported due to their superior properties of long-life operation and devoid of friction-induced heat and abrasion. However, even though high performance of e-REHs with both the operation modes has been achieved, the selection criteria and different connection schemes have not been well investigated. As far as we have searched, there was no study to exploit the overall theoretical modeling of different working modes and connection schemes. Furthermore, even though the disk-shaped e-REH have been intensively investigated as a power generation unit [53,67], their integration with ball bearing to achieve a ultra-high-precision and a self-powered speed sensor has never been reported.

In this paper, we propose an e-REH with bipolar-charged electrets for boosting its output performance. High-resolution and uniform-potential micro charges are obtained with a selectively localized corona discharging method, which has implanted both positive and negative charges into a single sheet of electret thin films. Both theoretical analysis and experimental studies using two types of operation modes, e.g., freestanding mode (Fe-REH) and sliding mode (Se-REH), are performed. To evaluate the performance using different operation modes, a generalized theoretical model of bipolar-charged e-REHs is derived with a function expression of surface charge density on the electret, capacitance, load resistance, and operating frequency (the number of sectors and the rotation rates). Results show that the power generation mechanism and capacitance are the two fundamental factors leading to the differences in the output performance. Finally, an intelligent thrust bearing based on the electret rotatory energy harvester is developed, which has self-powered and self-sensing capabilities. Instead of the amplitudes of output voltages, we use the response frequencies to monitor the rotational speeds of the thrust bearing. Ultra-high sensitivity and excellent linearity are successfully achieved. This study provides a foundation technology for the realization of high-precision bearing sensing.

2. DEVICE CONCEPTUALIZATION AND EXPERIMENTAL METHODS

2.1 Device conceptualization

The concept of e-REH with bipolar-charged electrets is originated from a permanent magnet generator using a reverse polarized magnet, such as the Three Gorges Dam in China (Fig. 1(a)). The history of harnessing wind and flowing water energy using electromagnetic windmills and hydropower stations dates back to many centuries ago. To maximize the power generation and magnetic flux variation, massive permanent magnets which are reversed magnetized are usually employed to convert kinetic energy to electrical energy (Fig. 1(b)). However, most reported e-REH devices are based on unipolar surface charge, either by positive or negative induction. There are two conventional modes of unipolar-charged electret rotatory energy harvesters: e.g., Fe-REH and Se-REH as shown in Figs. 1(c) and 1(d), respectively.

In analogy to the conventional hydropower generator with reverse polarized magnets of N poles and S poles, the proposed disk-shaped electret power generator has both positive and negative charged electrets integrated into a single rotational energy conversion system (Fig. 1(e)). The generator with a two-layer structure is divided into two parts: a movable rotator and an immovable stator. Eight fan-shaped electrodes with a center angle of 22.5° is patterned with printed circuit board (PCB) technology onto an Acrylonitrile Butadiene Styrene (ABS) disk. The electret thin film is bonded onto the stator and then micro-patterned with positive and negative charges through a selectively localized corona discharging process. One end of the external circuit is connected to the bottom electrode which is below both positive and negative charged electret, whereas the other end is connected to the top rotary plate with eight fan electrode. Based on this design, the induced net charge in the top rotary plate can be varied from a positive maximum to a negative maximum (Fig. 1(e)), whereas it is well-known that the charge can only be changed from positive maximum to quasi-zero status for the conventional single-charged electret harvester (Fig. 1(c-d)). Details of the power enhancement mechanism will be further deliberated in the following sections.

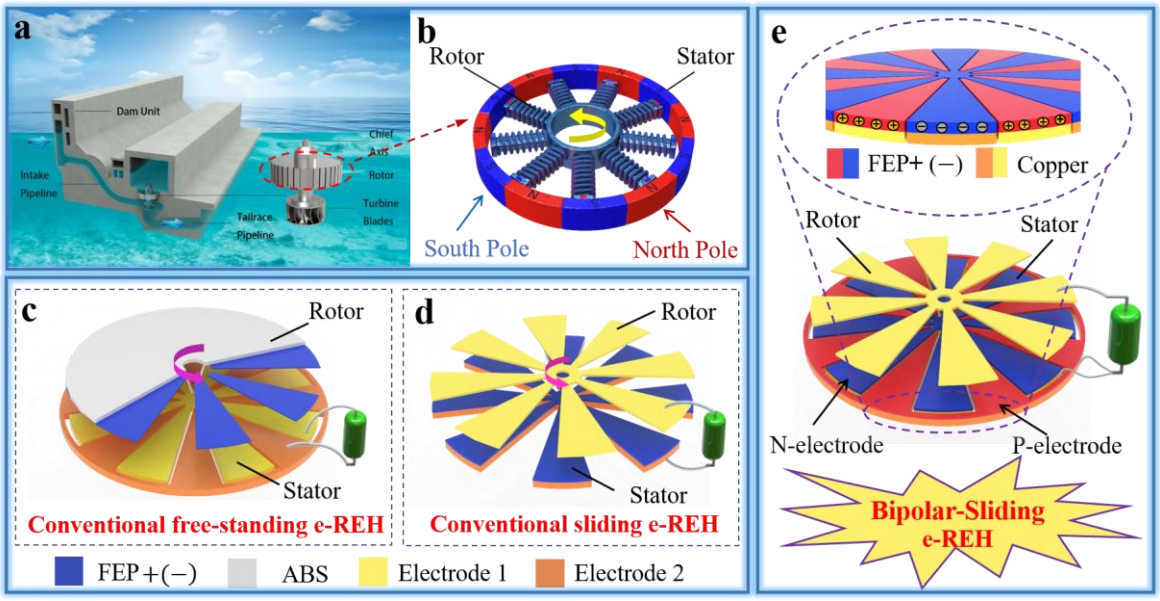

Fig. 1. (a-b) 3-D schematic of electromagnetic hydropower station with reverse polarized magnets with N poles and S poles alternately distributed in a ring. (c-d) Schematic and connection scheme of conventional freestanding e-REH (Fe-REH) and sliding e-REH (Se-REH). (e) New concept and connection scheme of Se-REH with bipolar-charged electrets

2.2 Selectively localized corona discharging process

To introduce charge distribution into the electret thin films, a selectively localized corona discharging system composed of a shadow mask and multiple discharge needles is developed (Fig. 2(a)). The electret-patterning method does not have any micro-patterning or etching process of the electret film itself. An array of tungsten needles, functioned as both discharge needles and a metallic grid in the conventional discharging process, are utilized to implant uniform charges into the electret material. Deep Reactive Ion Etching (DRIE) process is used to form an array of micro-scale openings in a silicon wafer, which is served as a shadow mask. This shadow mask is then deposited with 300 nm gold as a conductive grid on the top and 500 nm silicon oxide as an insulation layer at the bottom. Finally, the electret thin film is selectively charged by placing the shadow mask on the top and the silicon substrate with a gold electrode at the bottom during the discharging process. The gap between the needle tips and the shadow mask is kept about 5~10 mm and the electrode on the substrate is connected to the ground.

For the bipolar discharging process, the electrets are first implanted with negative charges and then with positive charges. During negative discharging, the voltages applied to needle and shadow mask voltages are kept around -3~ -4 kV and -300 V, respectively (Fig. 2(a)). Therefore, the negative ions generated at the needle tips are forced to move to the lower potential electrode on the substrate and then are implanted into the electrets through the predefined holes. Therefore, the exposed area of electrets is implanted with the negative charges. After this process, the shadow mask is rotated to shield the negatively pre-charged area and expose the uncharged areas. Conversely, the voltages applied to needle and shadow mask are switched to around +3~ +4 kV and +300 V in the positive discharging process, respectively (Fig. 2(b)).

Fig. 2(c) shows the measured potential distribution of the fan-shaped charges using a 3D surface potential scanner. The blue and red colors represent the negatively and positively charged areas, respectively. It can be seen that the blue and red colors are quite distinct from each other with a uniform depth, indicating that both the negative and positive charges are successfully implanted and excellent surface potentials are achieved. Scanning electron microscopy (SEM) is utilized to observe high-resolution micro-sized charge patterns in LDPE electret thin films using the localized corona discharging method, and the obtained images are shown in Figs. 2(d) and 2(e). The arbitrary shape of charge distribution can be readily achieved by changing the pattern of the shadow mask. The bright and dark areas correspond to the negatively charged and the uncharged regions, respectively. Good uniformity of charge distribution with a high-resolution is achieved.

Fig. 2(f) shows surface potential evolution of bipolar-charged electrets at the room temperature over a period of 96 hours. The electret surface potential decreases sharply from 1500 V to around 1200 V on the first day, but the decrease rate reduces sharply afterwards. After 72 hours, the negatively and positively charged are still maintain surface potentials of -1120 V and 620 V, respectively. The difference between these two results is mainly due to a more substantial storage capacity for the negative charges of FEP electret material than that of positive charges.

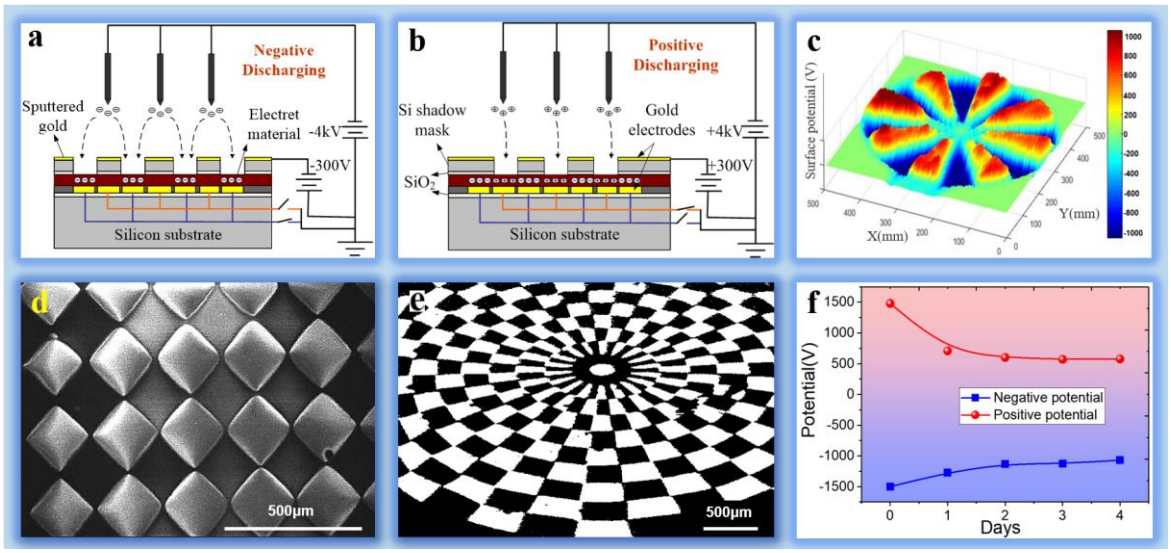

Fig. 2. Selectively localized corona discharging system using shadow masks: (a) Negative discharging process. (b) Positive discharging process. (c) 3D surface potential mapping of fan-shaped charge distribution by bipolar discharging. (d-e) SEM images of periodic micro-patterned square and circular charges in the electrets (negative charged). (f) The surface potential stability evolution of bipolar-charged electrets at the room temperature over a period of 96 hours.

3. OPERATING PRINCIPLE AND MODELING

3.1. Operating principle

Fig. 3 shows the operating principle and charge circulations of proposed unipolar and bipolar-charged e-REHs. To facilitate the observation of charge flow states, the electric fields and surface potentials of electrets are visualized using the results obtained from the Comsol Multiphysics simulation with the electrostatic module (es module). Figs. 3(a) and 3(b) show three different operation states of the proposed unipolar-charged e-REH and its corresponding charge flowing states, respectively. At the initial condition (State I), the rotor electrode is completely separated from the negatively charged electret. There is no net charge induced in this state. The charges begin to accumulate in the rotor electrode when the rotor starts to rotate with an angle of θ° (State II). The charges continue to flow in the same direction until reach their maximum value when the rotor and the stator electrodes are

fully overlapping with each other (State III). During a charge circulation cycle, the charge induced in the rotor electrode is varied from zero to its maximum value ($+Q_{max}$).

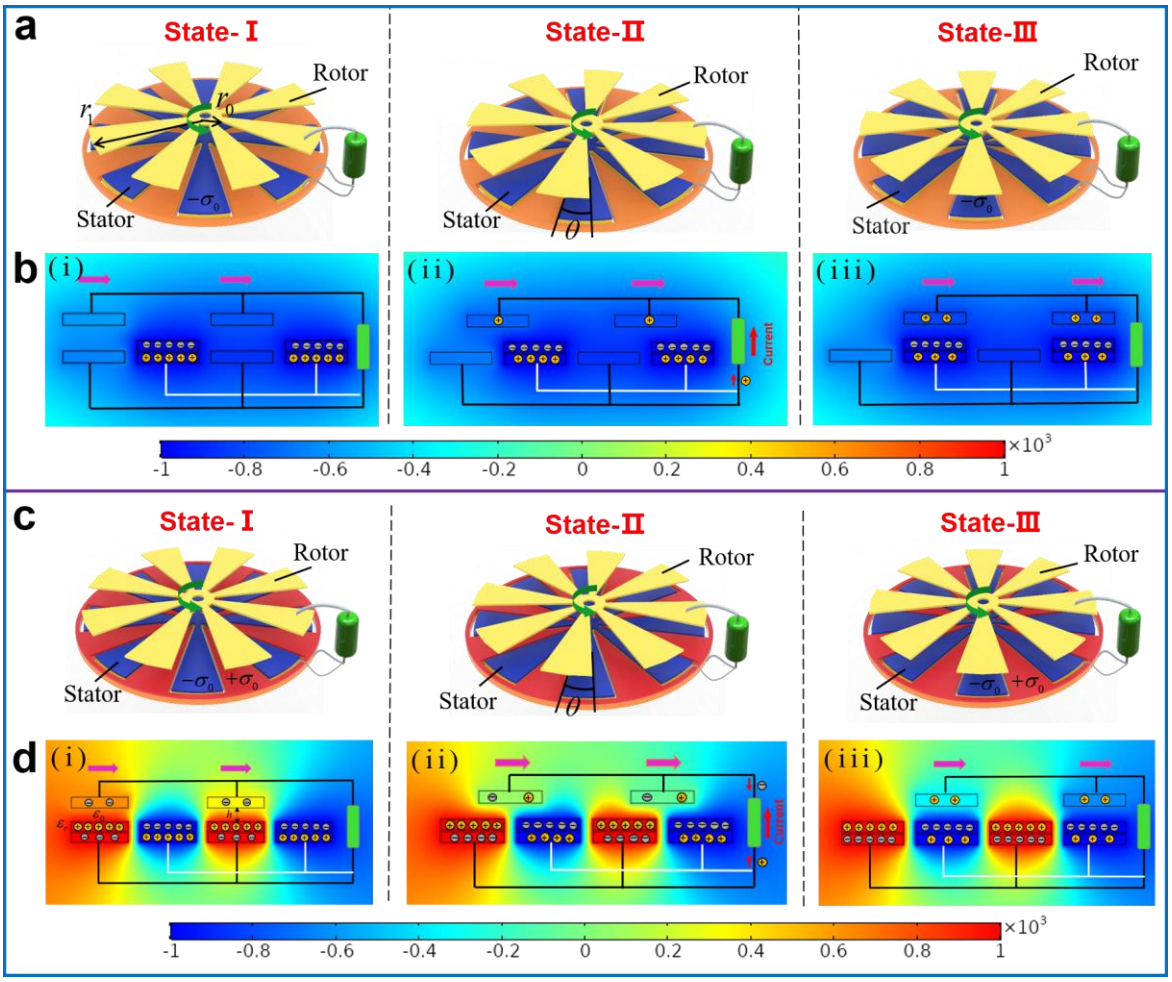

Fig. 3. The operating principle and charge circulations of unipolar-charged e-REH and proposed bipolar-charged e-REH: (a) Schematic diagram of the unipolar-charged e-REH at three operation states. (b) Electric contour simulation and charge flow of the unipolar-charged e-REH at three operation states. (c) Schematic diagram of the bipolar-charged e-REH at three operation states. (d) Electric contour simulation and charge flow of the bipolar-charged e-REH at three operation states.

Figs. 3(c) and 3(d) show three different operation states of the newly proposed bipolar-charged e-REH and its corresponding charge flowing states, respectively. The charge circulation process is similar to that of unipolar-charged e-REH. The main difference is that the fan-shaped electrodes of the rotor are firstly 100% overlapped with the positively

charged areas in the stator(State I), and then changed to 100% overlapped with the negatively charged areas in the stator (State III). Therefore, the overall transferred charges in the rotor are varied from the negative maximum ($-Q_{max}$) to the positive maximum ($+Q_{max}$) for the bipolar-charged electrets, whereas it only changes from zero to positive maximum ($+Q_{max}$). Assuming that the positively and negatively charged regions of the electrets have the same surface charge density and uniform charge distribution, then the amounts of transferred charges with the bipolar-charged e-REH will be doubled of those for the unipolar-charged device. Therefore, according to a rough estimation using the relationship of $P \propto CV^2$, the power generated from the bipolar e-REHs can be enhanced by four times compared with that from the unipolar ones.

3.2. Modeling of unipolar and bipolar e-REHs

This section will investigate the performance of the unipolar and bipolar e-REHs with sliding mode through theoretical modeling analysis. The surface potential of the charged electret film is defined as V_0, which can be expressed by the charge stored in the electret film Q_0 and the capacitance of the electret C_0, as shown in Eq. (1):

$$V_0 = \frac{Q_0}{C_0} \tag{1}$$

The stored charge in the electrets can also be expressed as:

$$Q_0 = \sigma_0 S \tag{2}$$

where σ_0 is the density of charges in the electret, S is the electret's surface area during the corona discharging process. The electret capacitance can be calculated using:

$$C = \frac{\varepsilon_r \varepsilon_0 S}{d_0} \tag{3}$$

where d_0 is the thickness of the electret film, ε_0 and ε_r are the vacuum permittivity and the dielectric constant of the electret, respectively. Substituting Eq. (2) and Eq. (3) into Eq.

(1), the charge density on the electret surface σ_0 can be obtained as:

$$\sigma_0 = \frac{\varepsilon_r \varepsilon_0 V_0}{d_0} \tag{4}$$

Therefore, the charge density σ_0 can be obtained by measuring the surface potential of the electrets. According to electrostatic induction, net charges would be induced in both the rotor electrodes and the stator electrodes by the electric charges stored in the electrets. The stator electrodes would attract much more charges than the rotor electrodes, since the stator is closer to the electrets. However, the charges transferred in the external circuit are essentially determined by the polarity changes of the induced charges in the rotor electrode. In contrast, most charges generated by the stator electrode are not transferred, equivalent to the locked charges. The effective charges are the charges induced on the rotor electrode. Therefore, the effective charge density in the rotor electrode is much smaller than the surface charge density on the electret. Based on the net charge density in the electret and the attenuation of the electric field in space, a modified inductance factor η is introduced to reflect the actual charge density σ induced on the rotor electrode:

$$\sigma = \eta \sigma_0 \tag{5}$$

At the initial position as shown in Fig. 3(c), the rotor is completely overlapped with the positively charged regions of the stator. Therefore, when the rotor electrode is rotated with an angle of θ, the charge induced on the rotor electrode $Q_E(\theta)$ can be expressed as:

$$Q_E(\theta) = \begin{cases} \frac{1}{2} n\sigma(r_1^2 - r_0^2)\theta + (-\sigma)\left[S_0 - \frac{1}{2} n(r_1^2 - r_0^2)\theta\right], & \theta \in \left[0\ ,\ \frac{\pi}{n}\right) \\ \sigma\left[2S_0 - \frac{1}{2} n(r_1^2 - r_0^2)\theta\right] + (-\sigma)\left[\frac{1}{2} n(r_1^2 - r_0^2)\theta - S_0\right], & \theta \in \left[\frac{\pi}{n}, \frac{2\pi}{n}\right] \end{cases} \tag{6}$$

where S_0 is the fan-shaped area of the rotor electrode, n is the number of fan-shaped blades of the rotor electrode, θ is the rotation angle from the initial moment ($t = 0$) to a certain moment, r_0 and r_1 are the inner and outer diameters of the rotor electrode,

respectively. The blade area S_0 and rotation angle θ can be expressed as:

$$S_0 = \frac{1}{2} n(r_1^2 - r_0^2)\theta_0 \tag{7}$$

$$\theta = \omega t \tag{8}$$

where θ_0 is the central angle of a fan-shaped blade of the rotor electrode ($\theta_0 = \pi/n$) and ω is the rotor electrode angular velocity. By substituting Eq. (7) and Eq. (8) into Eq. (6), $Q_E(t)$ can be simplified as:

$$Q_E(t) = \begin{cases} \frac{1}{2} n\sigma(r_1^2 - r_0^2)(2\omega t - \theta_0), & t \in \left[0, \frac{\pi}{n\omega}\right) \\ \frac{1}{2} n\sigma(r_1^2 - r_0^2)(3\theta_0 - 2\omega t), & t \in \left[\frac{\pi}{n\omega}, \frac{2\pi}{n\omega}\right] \end{cases} \tag{9}$$

Since the air gap between the rotor and the stator electrodes is much smaller than that of blade area, the capacitance between the two electrodes can be approximated as a parallel plate capacitance by ignoring the fringing effect. The capacitance between the stator and the rotor electrodes can be obtained:

$$C = \frac{\varepsilon_0 \pi (r_1^2 - r_0^2)}{2\left(\frac{d_0}{\varepsilon_r} + h\right)} \tag{10}$$

where h is the distance between the rotor and the stator of bipolar e-REH. Therefore, the induced potential difference(U_E) between the two electrodes by the induced charges can be expressed as:

$$U_E(t) = \begin{cases} \dfrac{n\sigma\left(\frac{d}{\varepsilon_r} + h\right)(2\omega t - \theta_0)}{\varepsilon_0 \pi}, & t \in \left[0, \frac{\pi}{n\omega}\right) \\ \dfrac{n\sigma\left(\frac{d}{\varepsilon_r} + h\right)(3\theta_0 - 2\omega t)}{\varepsilon_0 \pi}, & t \in \left[\frac{\pi}{n\omega}, \frac{2\pi}{n\omega}\right] \end{cases} \tag{11}$$

The e-REH can be considered as an ideal AC voltage source and a capacitor in series, as shown in Supporting Information Fig. S1(a). The charge flow can be calculated using the differential equation based on the Kirchhoff's voltage law:

$$R\frac{dQ(t)}{dt}=-\frac{1}{C}\times Q(t)+U_E(t) \tag{12}$$

Solving the differential Eq. (9) with considering the initial boundary condition $Q_{(t=0)}+Q_{(t=\frac{\pi}{n\omega})}=0$ and the periodic boundary condition $Q_{(t=0)}=Q_{(t=\frac{2\pi}{nw})}$, the charge variation between the two electrodes during a single period can be expressed as:

$$Q(t)=\begin{cases} n\sigma(r_1^2-r_2^2)(wt-\frac{\theta_0}{2})-\sigma(r_1^2-r_2^2)n\omega RC\left[1-\frac{2\exp\left(-\frac{t}{RC}\right)}{1+\exp\left(-\frac{\pi}{n\omega RC}\right)}\right], & t\in\left[0\ ,\ \frac{\pi}{n\omega}\right) \\ n\sigma(r_1^2-r_2^2)(\frac{3\theta_0}{2}-\omega t)+\sigma(r_1^2-r_2^2)n\omega RC\left[1-\frac{2\exp\left(\frac{\pi}{n\omega RC}-\frac{t}{RC}\right)}{1+\exp\left(-\frac{\pi}{n\omega RC}\right)}\right], & t\in\left[\frac{\pi}{n\omega}\ ,\ \frac{2\pi}{n\omega}\right] \end{cases} \tag{13}$$

By taking the derivative of the time on both sides of Eq.(13), the output current $i(t)$ during a single period can be expressed as:

$$i(t)=\begin{cases} 2\sigma\left(r_1^2-r_0^2\right)n\omega\left[\frac{1}{2}-\frac{\exp\left(-\frac{t}{RC}\right)}{1+\exp\left(-\frac{\pi}{n\omega RC}\right)}\right], & t\in\left[0,\frac{\pi}{n\omega}\right) \\ -2\sigma\left(r_1^2-r_0^2\right)n\omega\left[\frac{1}{2}-\frac{\exp\left(\frac{\pi}{n\omega RC}-\frac{t}{RC}\right)}{1+\exp\left(-\frac{\pi}{n\omega RC}\right)}\right], & t\in\left[\frac{\pi}{n\omega},\frac{2\pi}{n\omega}\right] \end{cases} \tag{14}$$

Multiplying the Taylor expansion of Eq.(14) and calculating the limit condition at R→0 and R→∞, the short-circuit current I_{sc} and the open-circuit voltage U_{oc} can be obtained, respectively:

$$I_{SC}=\begin{cases}\sigma\left(r^2-r_0^2\right)n\omega, & t\in\left[0,\dfrac{\pi}{n\omega}\right)\\ -\sigma\left(r^2-r_0^2\right)nw, & t\in\left[\dfrac{\pi}{n\omega},\dfrac{2\pi}{n\omega}\right]\end{cases} \tag{15}$$

$$U_{OC}=\begin{cases}\dfrac{\sigma\left(r_1^2-r_0^2\right)}{2C}(2n\omega t-\pi), & t\in\left[0,\dfrac{\pi}{n\omega}\right)\\ -\dfrac{\sigma\left(r_1^2-r_0^2\right)}{2C}(2n\omega t-3\pi), & t\in\left[\dfrac{\pi}{n\omega},\dfrac{2\pi}{n\omega}\right]\end{cases} \tag{16}$$

The average output power P_{av} of the bipolar e-REH can be defined by the following equation:

$$P_{av}=\frac{\int_0^T i(t)^2 Rdt}{T},T=\frac{2\pi}{n\omega} \tag{17}$$

By substituting $i(t)$ into Eq. (17), the average output power P_{av} can be obtained as:

$$P_{av}=\frac{4\sigma^2\left(r^2-r_0^2\right)^2 n\omega}{C}\left\{\frac{n\omega RC}{4}+\frac{(n\omega RC)^2}{2\pi}\left[1-\frac{2}{1+\exp\left(-\dfrac{\pi}{n\omega RC}\right)}\right]\right\} \tag{18}$$

The above theoretical derivation is the analysis of the working principle of bipolar e-REH device. For unipolar e-REH, the details of the related modeling can be found in Supporting Information Section 1. After comparing and analyzing theoretical results of the unipolar-charged e-REH, , we can conclude that the two deductions have certain similarities, which can be summarized by the following formula:

$$i(t)=\begin{cases} k\sigma\left(r_1^2-r_0^2\right)n\omega\left[\dfrac{1}{2}-\dfrac{\exp\left(-\dfrac{t}{RC}\right)}{1+\exp\left(-\dfrac{\pi}{n\omega RC}\right)}\right], & t\in\left[0,\dfrac{\pi}{n\omega}\right) \\ -k\sigma\left(r_1^2-r_0^2\right)n\omega\left[\dfrac{1}{2}-\dfrac{\exp\left(\dfrac{\pi}{n\omega RC}-\dfrac{t}{RC}\right)}{1+\exp\left(-\dfrac{\pi}{n\omega RC}\right)}\right], & t\in\left[\dfrac{\pi}{n\omega},\dfrac{2\pi}{n\omega}\right] \end{cases} \tag{19}$$

$$P_{av}=\frac{k^2\sigma^2\left(r^2-r_0^2\right)^2 n\omega}{C}\left\{\frac{n\omega RC}{4}+\frac{(n\omega RC)^2}{2\pi}\left[1-\frac{2}{1+\exp\left(-\dfrac{\pi}{n\omega RC}\right)}\right]\right\} \tag{20}$$

where the discharging factor k is related to the discharging method, such as unipolar discharging (k=1) and bipolar discharging (k=2). According to Eq. (20), the average output power of e-REH is affected by the induced charge density on the electrode, the number and size of the fan blades, the angular velocity of the rotor electrode, and the influence of load resistance and capacitance between two electrodes. By increasing the discharging factor k from 1 to 2 with bipolar-charged electrets, the output current and the average output power are increased up to 200% and 400% compared with those of the unipolar e-REH, respectively.

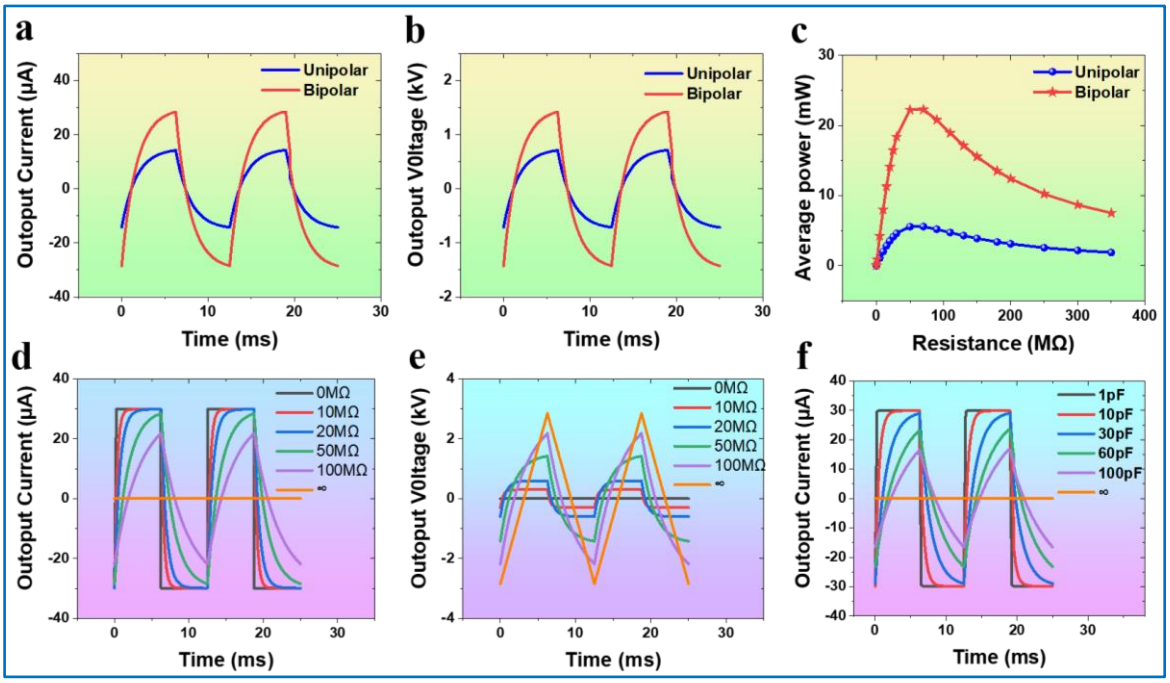

Fig. 4. Modeling results of unipolar and bipolar e-REHs: (a-c) Comparisons of output voltages, currents and powers of unipolar and bipolar e-REHs with speed of 600 rpm and load resistance of 50MΩ. (d-e) Output current and voltage waveforms of the bipolar e-REH with different external load resistances at 600 rpm. (f) Output current waveforms of the bipolar e-REH with different capacitances at speed of 600 rpm and resistance of 50MΩ.

By substituting the data in Supporting Information Table 1 into Eq. (19) and Eq. (20), the modeling results of unipolar and bipolar e-REHs can be obtained, and the results are shown in Fig. 4. Figs. 4(a) and 4(b) show the output voltage and current wavforms of unipolar and bipolar e-REHs with a speed of 600 rpm and a load resistance of 50 MΩ, repectively. Clearly, the output voltage and output current of the bipolar e-REH are theoretically twice those of the unipolar e-REH. The waveforms of both the bipolar-charged and the unipolar-charged e-REHs follow a similar output trajectory. Fig. 4(c) shows the resistance optimization processes of the unipolar-charged and the bipolar-charged e-REHs. The optimal output powers of the unipolar-charged and the bipolar-charged e-REHs are 5.6 mW at 60 MΩ and 22.4 mW at 60 MΩ, respectively. This clearly demonstrate that there is a four-times increase of output power after using the bipolar-charged method.

Figs. 4(d) and 4(e) show the output current and voltage waveforms of the bipolar e-REH with different external load resistances at a rotation speed of 600 rpm. When a short circuit (R = 0 Ω) occurs, there is no delay in the charge transfer and a square waveform is generated. As the load resistance increases, the effect on current limitation is gradually strengthened. The charge transfer produces a time lag effect, which results in that the output current waveform gradually becomes a sine wave-like output. When the open circuit takes place ($R \rightarrow \infty$), the load resistance blocks the current. The charge cannot be transferred, leading to a zero output current. The output voltage waveforms exhibit remarkably different pattern. As the load resistance is increased, the output voltages at both ends of the load resistance are gradually increased. When the circuit is open ($R \rightarrow \infty$), the waveform shows a triangular wave since the internal resistance of the e-REH is negligible compared to the external load resistance.

Fig. 4(f) shows the output current waveforms of the bipolar e-REH with different capacitances at a speed of 600 rpm and a resistance of 50 MΩ. The charge storage capacity of the capacitor is extremely low when the capacitance is 1 pF. At this condition, the output voltage reaches its maximum value and the output current waveform exhibits an approximately square wave. As the capacitance increases, the charge storage capacity of the capacitor is gradually increased. The charge transfer produces a time lag effect, making the output current to evolve into a sinewave-like waveform. When the capacitance is infinite ($C \rightarrow \infty$), the charge storage capacity of the capacitor becomes infinite and the value of output current decreases to 0 A. However, the surface charge density of the positively and negatively charged regions of electrets can hardly maintain the same in actual discharging process. Therefore, the theoretical model based on different surface charge densities of the positive and negative charged regions are derived and calculated in Supporting Information Section 2. Supporting Information Fig. S2 shows the modeling results of e-REHs under different charge densities of unipolar and bipolar e-REHs with a speed of 600 rpm and load resistance of 50MΩ.

3.3. Modeling of Fe-REH and Se-REH modes

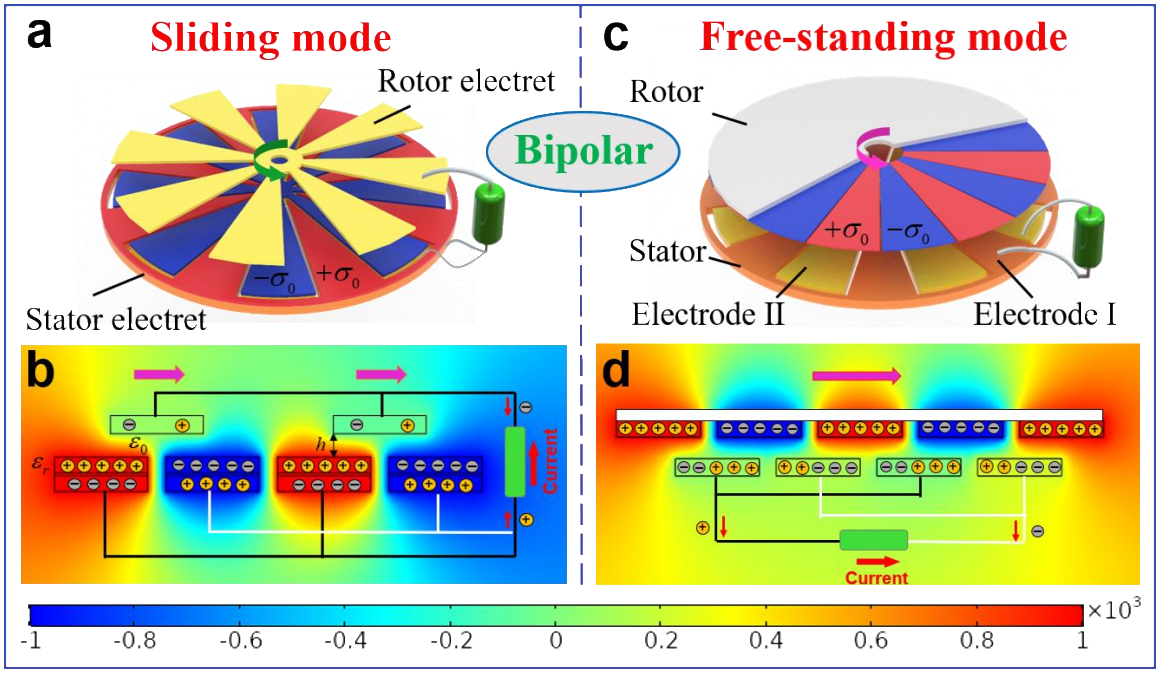

Fig. 5. The operating principle and charge circulations of the bipolar-charged e-REH in sliding mode (Se-REH) and freestanding mode (Fe-REH): (a) Structure design and wire connection scheme of bipolar-charged Se-REH. (b) Electric contour simulation and charge flow of bipolar-charged Se-REH. (c) Structure and wire connection of bipolar-charged Fe-REH. (d) Electric contour simulation and charge flow of bipolar-charged Fe-REH.

This section focuses on the modeling and analysis of the e-REH in both the freestanding mode (Fe-REH) and the sliding mode (Se-REH). Fig. 5 shows the operating principles and charge circulations for the bipolar-charged e-REH in both sliding mode (Se-REH) and freestanding mode (Fe-REH). For the bipolar-charged Se-REH, one end of the load resistance is connected to the rotor electrode, the other end is connected to the negative and positive electrodes on the stator. For the bipolar-charged Fe-REH, both two ends of the load resistance are connected to the stator electrodes. When the rotor rotates with an angle θ, the overall transferred charge varies from negative maximum ($-Q_{max}$) to positive maximum ($+Q_{max}$) for the bipolar-charged electrets.

For the bipolar-charged Fe-REH shown in Fig. 5(d), when the rotor rotates an angle θ, according to the principle of electrostatic induction, the charge $Q(\theta)$ induced in the

Electrode I can also be expressed using Eq.(9). However, the charge $Q(\theta)$ is the charge induced on the Electrode I on the stator of the the bipolar-charged Fe-REH instead of the charge induced on the rotor electrode of the bipolar-charged Se-REH. Due to the differences of the e-REH in these two modes are mainly concentrated in the structure and the connection between the electrodes, the capacitance values between two electrodes are completely different in these two modes. For the bipolar-charged Se-REH, the capacitance C refers to the capacitance between the rotor electrode and the stator electrode, which can be expressed by Eq. (10). However, for the bipolar-charged Fe-REH, the capacitance C_1 refers to the capacitance between Electrode I and Electrode II of the interdigital electrode. After measurement, the capacitance C_1 between Electrode I and Electrode II is fixed (e.g., 60 pF).

The previous section (Section 3.2) has already shown the modeling and analysis results of the e-REH in the sliding mode. Because the essential working principles of the e-REH in the two modes are based on the principle of electrostatic induction, there is a derivation process similar to the previous section for the modeling and analysis process of the e-REH in a free-standing mode. Supporting Information Section 3 shows the similar derivation parts of the theoretical modeling of bipolar-charged Fe-REH. The analysis conclusions of output currents and powers are as follows:

$$i(t)=\begin{cases} 2\sigma\left(r_1^2-r_0^2\right)n\omega\left[\dfrac{1}{2}-\dfrac{\exp\left(-\dfrac{t}{RC_1}\right)}{1+\exp\left(-\dfrac{\pi}{n\omega RC_1}\right)}\right], t\in\left[0,\dfrac{\pi}{n\omega}\right) \\ -2\sigma\left(r_1^2-r_0^2\right)n\omega\left[\dfrac{1}{2}-\dfrac{\exp\left(\dfrac{\pi}{n\omega RC_1}-\dfrac{t}{RC_1}\right)}{1+\exp\left(-\dfrac{\pi}{n\omega RC_1}\right)}\right], t\in\left[\dfrac{\pi}{n\omega},\dfrac{2\pi}{n\omega}\right] \end{cases} \tag{21}$$

$$P_{av} = \frac{4\sigma^2\left(r^2 - r_0^2\right)^2 n\omega}{C_1}\left\{\frac{n\omega RC_1}{4} + \frac{(n\omega RC_1)^2}{2\pi}\left[1 - \frac{2}{1+\exp\left(-\frac{\pi}{n\omega RC_1}\right)}\right]\right\} \quad (22)$$

By comparing Eq. (18) and Eq. (22), it is found that the theoretical modeling and analysis results of the bipolar charged Fe-REH are basically the same as the theoretical results of the bipolar charged Se-REH. However, there are some differences between the two working modes. For the bipolar-charged Fe-REH, the capacitance between the two interdigital electrode networks on a printed circuit board (PCB) is a fixed value, which is 60 pF measured by a precision LCR meter (Applent AT811, CN). On the other hand, for the bipolar-charged Se-REH, the capacitance between the rotor electrode and the stator electrode of Se-REH can be adjusted by adjusting the gap between the two electrodes. The relationship between the capacitance and gap of the rotor electrode and the stator electrode for Se-REH is sketched in Supporting Information Fig. S1(b), which indicates that the capacitance between the two electrodes decreases as the distance increases. When the gap is 1mm, the capacitance between the two electrodes of Se-REH is 54 pF, which is very close to the measured capacitance of the Fe-REH.

3.4. Summary of the modeling

The theoretical results of the bipolar-charged e-REH with sliding and free-standing operation modes is shown in Fig. 6. The theoretical derivations of e-REH in the two operating modes are the same by comparing Eq. (18) and Eq. (29), and the only affecting factor is the different capacitance variation conditions. Figs. 6(a-b) show the average output powers with different load resistances and capacitances. With the load capacitance increases from 15 pF to 90 pF, the optimal output power decreases from 72.5 mW to 12 mW. The optimal load resistance decreases from 130 MΩ to 22 MΩ. That indicates that the initial parasitic capacitance accounts for a large proportion of overall capacitance variaitons, which plays a vital role in the overall output performance and optimal load resistance. The larger the initial parasitic capacitance, the smaller the output power and optimal load resistance.

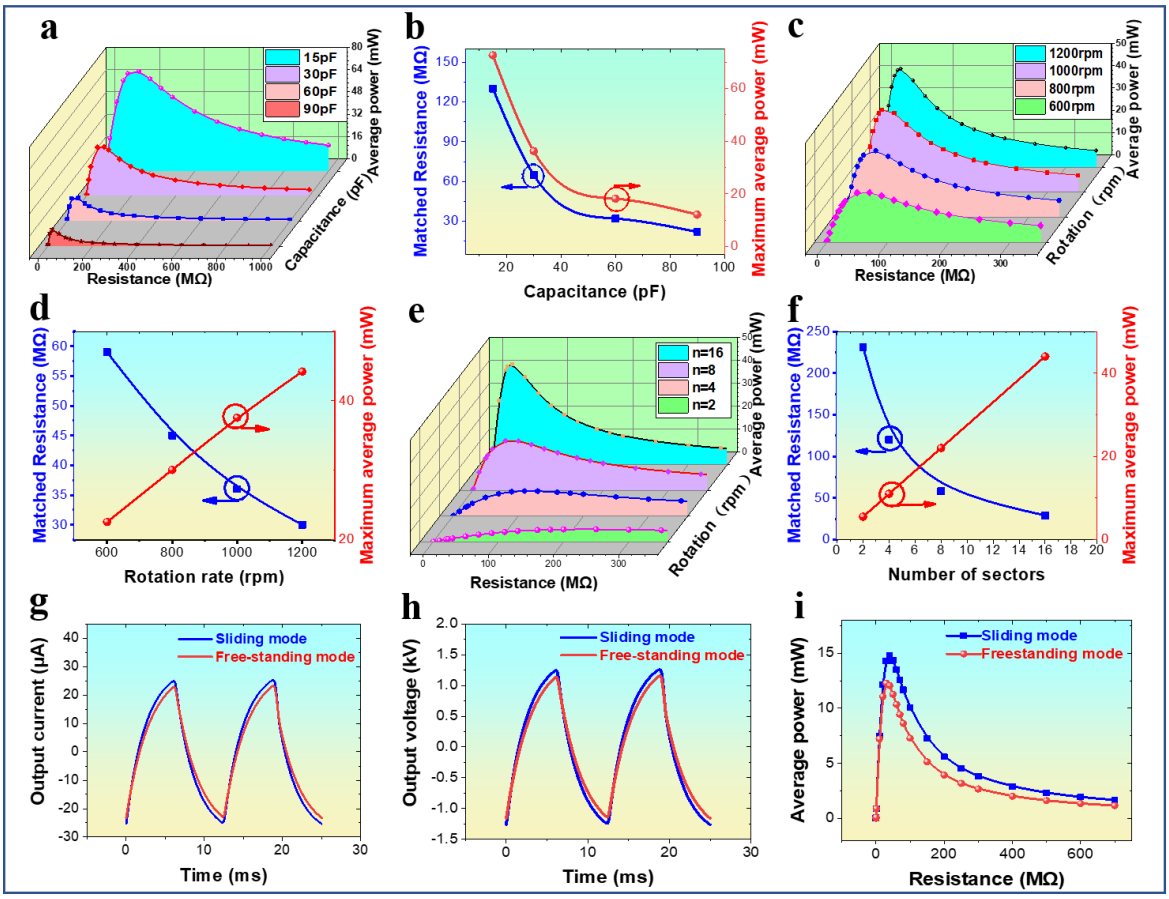

Fig. 6. Overall output performance of the bipolar-charged e-REH with sliding and free-standing operation modes: (a) The average output powers with different load resistances and capacitances. (b) Matched load resistances and maximum average power versus different capacitance. (c) The average output powers with different load resistances and rotation rates. (d) Matched load resistances and maximum average power versus different rotation rates. (e) The average output powers of Se-REH with different load resistances and the number of sectors. (f) Matched resistance and maximum average power of Se-REH versus the number of sectors. (g-i) Output current, voltage and average power with sliding and free-standing operation modes.

Figs. 6(c-d) show the average output powers with different load resistances and rotation rates.The comparison results of the average output powers and the load resistances at various rotation rates are sketched in Fig. 6(c), which indicates that the output power of e-REH also increases as the rotation rates increases. In the process of the output power changing with the load resistance, there is always a load resistance that maximizes the

average output power of e-REH. The relation of matched load resistance and the maximum average power at various rotation rates is sketched in Fig. 6(d). As the speed increases, the maximum average output power gradually increases, but the matching resistance continues to decrease because of the diminution of the capacitive reactance due to the increase in the output current frequency.

The comparison results of the average output powers and the load resistances in Se-REH at various number of sectors are sketched in Fig. 6(e), which indicates that the output power of Se-REH increases as the number of sectors increases. The relation of matched load resistance and the maximum average power of Se-REH with various the number of sectors is sketched in Fig. 6(f). As the number of sectors increases, the maximum average output power gradually increases. Still, the matching resistance continues to decrease because of the diminution of the capacitive reactance due to the increase in the output current frequency.

The different output performance of the bipolar charged Se-REH and Se-REH is compared by introducing the actual measured capacitance to calculate. The comparison of the Se-REH and Fe-REH output current and voltage is sketched in Fig. 6(g) and Fig. 6(h), respectively. When the gap of the rotor electrode and the stator electrode is 1 mm in sliding mode, the capacitance between the two electrodes is 54 pF, which is less than 60 pF in the freestanding mode. Therefore, the output current and voltage of the e-REH in the sliding mode are slightly higher than those in the freestanding mode. The comparison of the average output power of the Se-REH and Fe-REH is sketched in Fig. 6(g), which indicates that the maximum average output power and matched resistance of the e-REH in the sliding mode are that in the freestanding mode.

4. RESULTS AND DISCUSSION

4.1 Characterization of unipolar and bipolar e-REH

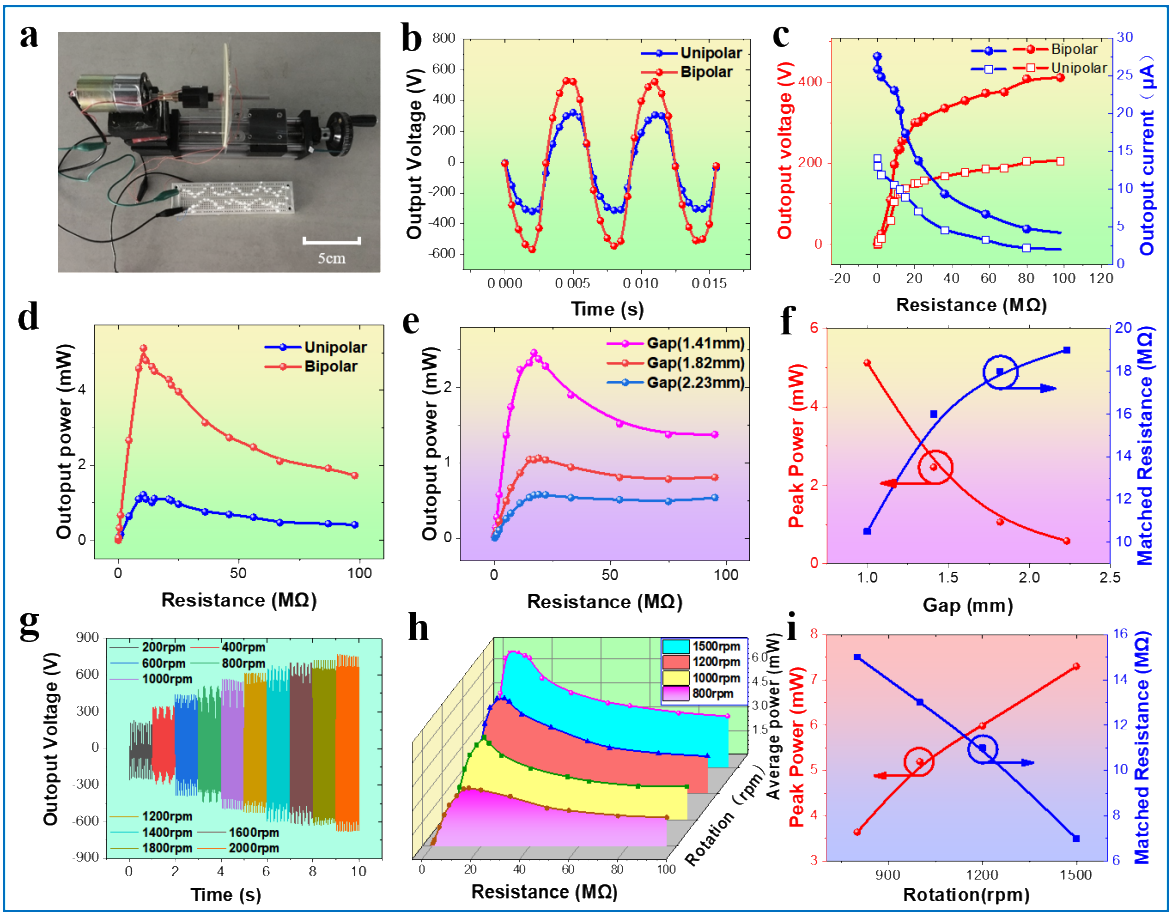

Fig. 7. Output performance of the e-REH in the sliding mode: (a) Experimental setup. (b) Output waveforms of unipolar and bipolar-charged e-REHs. (c-d) Output voltages, currents and powers of unipolar and bipolar-charged e-REHs with various load resistances. (e-f) Average power optimizations and output power peak magnitudes of bipolar-charged e-REH with different air gaps and load resistances. (g) Output voltages at various rotation speeds. (h) Power optimizations with different rotation speeds and load resistances. (i) Optimal load resistances and maximum average output powers at different rotation speeds.

The experimental setup with Se-REH is shown in Fig. 7(a). The diameter of the fabricated e-REH device is 100 mm. The e-REH device's stator is fixed onto the ball-screw guided structure, where its displacement can be adjusted accurately. The rotator of the e-REH device is connected to a rotatory motor whose rotation speed can be fully controlled. Both

the stator and the rotor are linked with the same shaft to achieve high coaxiality and stability. It is seen that 72 LEDs are lit up simultaneously by the system at a rotation speed of 1200 rpm. Fig. 7(b) shows comparisons of the output voltage waveforms for the unipolar and bipolar-charged e-REHs. The maximum output voltages of unipolar and bipolar-charged e-REH devices are 321.5V and 613.5V at 1200 rpm with the load resistance of 50 MΩ, respectively, indicating an increase of 91.0% output voltage with the proposed bipolar charged method. Comparisons of output voltages, output currents and average output powers of the unipolar and bipolar-charged e-REHs with different load resistances are shown in Figs. 7(c) and 7(d), respectively. The output currents and voltages of the bipolar-charged e-REH are almost twice those of the unipolar one. The maximum output powers of 1.29 mW and 5.06 mW are obtained for the unipolar and bipolar-charged e-REHs at a load resistance of 18 MΩ, respectively, which indicates the maximum output power of the bipolar e-REH is increased to 392.2% compared to those of the positive alone and negative alone configurations. These results drawn from experiments are well consistent with the theoretical calculations and the small difference may be due to the inhomogeneity of the charge distribution of the bipolar polarization in the experiment.

The average power optimizations and output power peak magnitudes of the bipolar-charged e-REH with different air gaps and load resistances are shown in Figs. 7(e) and 7(f). It is found that with an increase the air gap between the stator and the rotor, the output performance drops rapidly, while the optimal resistances are increased. Therefore, a larger capacitance variation will result in a lower optimum impedance according to the impedance expression $R \propto 1/j\omega C$ [30], where ω and C are the frequency and capacitance, respectively.

Figs. 7(g-i) show the output characteristics of bipolar-charged e-REH with different rotation speeds and load resistances. The output voltages and powers generally have a positive correlation with the rotation speed. The maximum output power of 6 mW has been obtained at the rotation speed of 1500 rpm and optimal resistance of 9.8 MΩ. The optimal load resistance is obtained at the highest rotation speed, which agrees with the results of theoretical modeling in Section 3.2.

4.2 Characterization of bipolar e-REH with different connection schemes

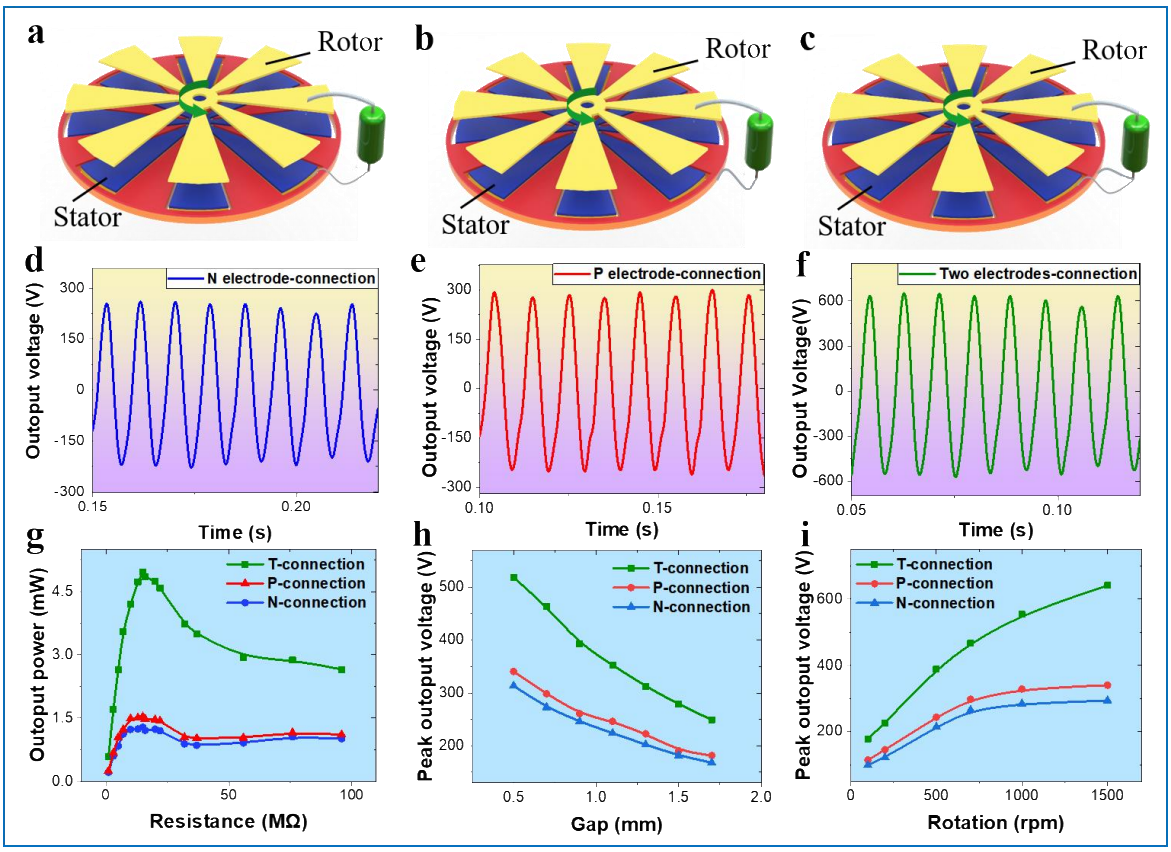

Fig. 8. Output characteristics of bipolar e-REH with different connection schemes: (a) Schematic diagram of bipolar e-REH with only N electrode connected. (b) Schematic diagram of bipolar e-REH with only P electrode connected. (c) Schematic diagram of bipolar e-REH with both N electrode and P electrode connected. (d-f) Output waveforms of bipolar e-REH with only N electrodes connected, only P electrodes connected and both electrodes connected. (g) Output power optimizations with different connection schemes at different load resistances. (h) Output power optimizations with different connection schemes at different air gap distances. (i) Peak output voltages with different connection schemes at different rotation speeds.

The output performance of bipolar-charged e-REH with different connection schemes has been further investigated. The bipolar-charged e-REH contains two independent electrodes, the N electrode and the P electrode, corresponding with negative and positive charged electrets below, respectively. Figs. 8(a-c) show schematics of three different circuit connection schemes, including only N-electrode connection (Fig. 8(a)), only P-electrode connection (Fig. 8(b)), both N- and P-electrodes connection (Fig. 8(c)). Figs. 8(d-f) show

the output voltage waveforms with the three corresponding three connection schemes with the rotation speeds of 1200 rpm at 50MΩ. It is shown that the voltage peak magnitudes of 282V, 321.5V and 652V are obtained with only N-electrode connection, only P-electrode connection and both N- and P-electrodes connection, respectively. The peak output voltage of both electrodes connected is about twice that of the N/P electrode connected alone. In addition, it is observed that the output waveform of both electrodes connected has a better symmetry in the positive and negative half axes.

Fig. 8(g) shows the comparison results of the average output power and the load resistance with different connection schemes. It is found the maximum output average power is 1.28 mW, 1.31 mW and 4.95 mW when the rotor electrode is connected to the P electrode, N electrode and both of two electrodes, respectively. Furthermore, the maximum average output power of connecting two electrodes is increased by 387% compared to that of connecting N electrode alone and 378% compared to that of connecting P electrode alone. Therefore, the different connection schemes of bipolar charged Se-REH in the sliding mode can achieve independent and stable energy supply. Figs. 8(h) and 8(i) show the output voltages with connection schemes at various air gaps and rotation speeds, respectively. The output voltages of the three connection schemes follow the same trends as depicted in Section 4.1, which are also consistent with the previous theoretical research conclusions.

4.3 Application in intelligent thrust ball bearing

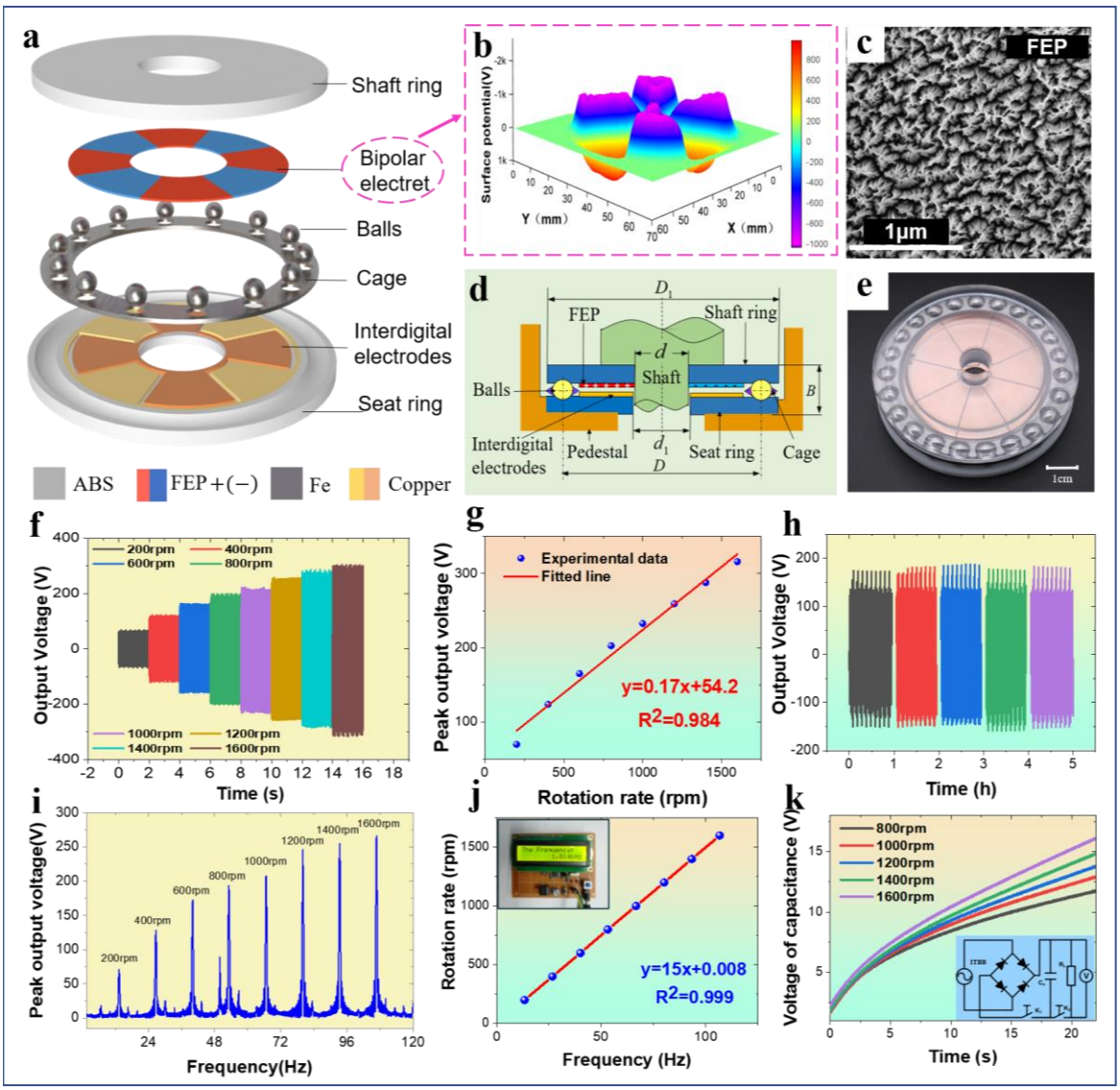

Fig. 9. Intelligent thrust ball bearing based on bipolar-charged e-REH (a) Structural explosion diagram of the ITBB. (b) Measured 3D potential distribution of the ITBB. (c) SEM image of the nano-structured electret surface. (d) Installation diagram of the ITBB with the rotor shaft and the bearing seat hole. (e) Physical photograph of the ITBB prototype. (f) Output voltage waveforms of ITBB at different rotation speeds. (g) Curve fitting of the magnitudes of output voltages as a function of different rotation speeds. (h) Durability test by operating the ITBB prototype at a rotation speed of 600 r/min for a period of 5 h. (i-j) Frequency domain response and curve fitting of ITBB as a function of ration speeds by Fast Fourier Transformation (FFT). (k) Capacitor charging circuit diagram and obtained 2.2 μF charging curves of using various ITBB rotation speeds of 800-1600 r/min.

Thrust ball bearing, as a particular type of rotary bearing, allows smooth rotation under high thrust loads at high-speed operations. They are widely used in slewing bearing arrangements for suspension struts, mining machines, and steering pivots of motor vehicles. Generally, the thrust bearing is composed of a shaft ring, cage, rolling balls, and seat ring. On the one hand, the shaft ring of the thrust ball bearing as a rotating part not only has a fixed gap with the seat ring but also has a relatively rotational movement with the seat ring. On the other hand, the rotor and stator of the e-REH in the freestanding mode possess non-contact and relative rotational motion characteristics, which are highly consistent with the operating mechanism of the shaft ring and the seat ring. Therefore, an intelligent thrust ball bearing (ITBB) integrating with the newly proposed e-REH device is proposed to achieve self-powered and self-sensing capabilities for the first time.

Fig. 9(a) shows the structural explosion diagram of the ITBB. It comprises six parts from top to bottom, including shaft ring, bipolar-charged electret, cage, rolling balls, interdigitated electrodes and seat ring, respectively. Due to the typical characteristics of non-contact and relative rotational movement, the proposed e-REH can be readily embedded into the ITBB to achieve self-powered and self-sensing capabilities.

The surface potential of the electret material is a crucial factor of ITBB for self-powered sensing applications. The measured 3D potential distribution of the fan-shaped rotational energy harvester is shown in Fig. 9(b). The blue and red areas are represented as the negative and positively charged areas, respectively. It is seen that bipolar distribution of positive and negative charges has been achieved by selectively localized corona discharging process. The SEM image of the nanostructured FEP surface is shown in Fig. 9(c). Fig. 9(d) shows the side view of the design of the proposed ITBB protype. The shaft ring of the ITBB rotates with the rotating shaft in the center. The seat ring is fixedly connected with the bearing housing hole. The cage separates the rolling steel balls evenly to guide the movement of the rolling balls. It prevents the balls from falling off, which guarantees the stability and smoothness of the thrust ball bearing during operation. The physical photograph of the fabricated ITBB prototype is shown in Fig. 9(e).

In the experiment, the frequency and amplitude of the output voltage are used to characterize the performance of ITBB at different rotation speeds. Fig. 9(f) shows the time-domain output voltage waveforms with the increased rotation speeds from 200 to 1600 rpm. The output voltage amplitude is further extracted and processed by a linear fitting. It is shown that the output voltage amplitude has a quasi-linear relationship with the rotation speeds at a slope of 0.17 (Fig. 9(g)). Fig. 9(h) shows the durability test results, which indicates a stable performance after operating at a speed of 600 r/min for 5 hours.

The time-domain output voltages are further transferred to a frequency-domain signal by using fast Fourier transform (FFT), and the results are shown in Fig. 9(i). It is found the frequency response has a superior-linear relationship with the rotation speed at a slope of 15. The linear factor is 99.9%, indicating an extremely high sensitivity and stability obtained (Fig. 9(j)). It has a much higher confidence level than that characterized by the amplitude of the output voltages. The output energy can also be used to charge a capacitor. Fig. 9(k) shows the capacitor charging circuit diagram and obtained 2.2 μF charging curves of using various ITBB rotation speeds of 800-1600 rpm. It is able to charge a 2.2 μF capacitor to a voltage of 17.2V within 22.5 s with the rotation speed of 1600 r/min, demonstrating its self-powered capability of the ITBB device.

As the core component of rotating machinery, thrust ball bearings are widely used in water conservancy generators, centrifuges, universal wheels, etc. Supporting Information Fig. S3 shows the integration of ITBB with a universal wheel in the trolley for energy harvesting and rotation angle detection applications. By a simple hand rotation drive, the ITBB can efficiently light up 75 × 55 mm^2 LCD with a logo of 'NPU' for nearly 5 seconds, as demonstrated in Supporting Information Video S1 and Fig. S4(a). Supporting Information Video S2 and Fig. S4(b) show the generated power of ITBB is capable of providing power for a series of temperature and humidity sensors at a high rotation speed driven by wind flow.

5. CONCLUSION

In this work, a bipolar-charged sliding-electret rotatory energy harvester(Se-REH) based on selectively localized corona discharging method is developed, which increases its output power by four times compared to Se-REH by unipolar charging theoretically. Through modeling and comparative analysis of the Se-REH and the Fe-REH, the clear analytical formulae of charge transfer, output current and average power in two operating modes are derived clearly, which is expressed as a function of surface charge density on the electret, capacitance, load resistance, and operating frequency (the number of sectors and the rotation rates). Due to the different structures and the connection between the electrodes for the Se-REH and the Fe-REH, the e-REH's capacitor in two operating modes is different, which is the fundamental factor leading to the difference in the output performance. Research shows that the capacitances of the e-REH in sliding mode and freestanding mode are 54 pF and 60 pF at a gap of 1mm between the rotor and the stator, which results in the output characteristics in two operating modes are pretty similar. In addition, a novel intelligent thrust bearing based on the bipolar-charged e-REH is proposed, which has self-powered and self-sensing capabilities. The rotation-to-frequency response of the ITBB has achieved an ultra-high frequency sensitivity of 15.0 rpm/Hz and a good linearity R2 (coefficient of determination) of 99.9%. The research outcomes have demonstrated the versatility and viability of proposed e-REH in various intelligent high-precision self-powered sensing and energy harvesting applications.

6. EXPERIMENTAL SECTION

Electret Surface Potential Characterization: Surface potential of the electret thin film is measured using a non-contact electrostatic voltmeter (Model347, Trek), and the probe-specimen distance is controlled within 1~3 mm. The probe of the electrostatic voltmeter is positioned on a 3D semi-automatic mobile platform to detect and record potential data at each point through step movement of the probe.

Fabrication of ITBB: The ITBB consists of six parts from top to bottom: shaft ring, FEP

electret thin film, balls, cage, interdigital electrodes and seat ring. The shaft ring and seat ring are designed by Solidworks Software and formed by 3D printing with ABS resin material. The ball is made of GCr15 special bearing steel with a standard diameter of 5mm. The cage is formed by laser cutting and processed by stamping and fitter. The interdigital electrode is processed by PCB process and embedded in the seat ring through interference fit. The FEP electret thin film is selectively charged and bonded onto the top of the electrode. The ITBB prototype is finally constructed through layer-by-layer assembly process.

Characterization of Bipolar e-REH: Rotation movement of power generation system is provided by a speed-controllable rotation motor (BLM230HP-ACS), whose rotation speed can be accurately adjusted. The electrical signal is recorded and displayed through a data acquisition system (DAQ, NI USB-6289 M series, USA), which is connected and controlled by a computer. The capacitance of the e-REH is measured using a precision LCR meter (Appellant AT811, CN).

ACKNOWLEDGEMENTS

This research is supported by the National Natural Science Foundation of China Grant (No. 51705429 & No. 61801525), the Fundamental Research Funds for the Central Universities, Guangdong Natural Science Funds Grant (2018A030313400), Space Science and Technology Foundation, Shenzhen Research Plan (JCYJ20180306171637410), 111 Project No. B13044, UK Engineering and Physical Sciences Research Council (EPSRC) for support under grant EP/P018998/1, International Exchange Grant (IEC/NSFC/201078) through Royal Society UK and the NSFC.

REFERENCES

[1] Z.L. Wang, Nanogenerators, self-powered systems, blue energy, piezotronics and piezo-phototronics – A recall on the original thoughts for coining these fields, Nano Energy, 54 (2018) 477-483.

[2] F.R. Fan, W. Tang, Z.L. Wang, Flexible nanogenerators for energy harvesting and self-powered electronics, Adv Mater, 28 (2016) 4283-4305.

[3] M.B. Khan, D.H. Kim, J.H. Han, H. Saif, H. Lee, Y. Lee, M. Kim, E. Jang, S.K. Hong,

D.J. Joe, Performance improvement of flexible piezoelectric energy harvester for irregular human motion with energy extraction enhancement circuit, Nano Energy, 58 (2019) 211-219.

[4] S. Cho, Y. Yun, S. Jang, Y. Ra, J.H. Choi, H.J. Hwang, D. Choi, D. Choi, Universal biomechanical energy harvesting from joint movements using a direction-switchable triboelectric nanogenerator, Nano Energy, 71 (2020) 104584.

[5] Y. Xi, H. Guo, Y. Zi, X. Li, J. Wang, J. Deng, S. Li, C. Hu, X. Cao, Z.L. Wang, Multifunctional TENG for blue energy scavenging and self-powered wind-speed sensor, Adv Energy Mater, 7 (2017) 1602397.

[6] Z. Wu, X. Yang, J. Wu, Conductive hydrogel- and organohydrogel-based stretchable sensors, ACS Appl Mater Interfaces, 13 (2021) 2128-2144

[7] K. Tao, J. Wu, L. Tang, L. Hu, S.W. Lye, J.J.J.o.M. Miao, Enhanced electrostatic vibrational energy harvesting using integrated opposite-charged electrets, Journal of Micromechanics and Microengineering, 27 (2017) 044002.

[8] X. Guo, Y. Zhang, K. Fan, C. Lee, F.J.E.C. Wang, A comprehensive study of non-linear air damping and "pull-in" effects on the electrostatic energy harvesters, Energy Conversion and Management, 203 (2019) 112264.

[9] K. Fan, J. Hao, C. Wang, C. Zhang, W. Wang, F. Wang, An eccentric mass-based rotational energy harvester for capturing ultralow-frequency mechanical energy, Energy Conversion and Management, 241 (2021) 114301.

[10] A. Luo, Y. Zhang, X. Dai, Y. Wang, W. Xu, Y. Lu, M. Wang, K. Fan, F. Wang, An inertial rotary energy harvester for vibrations at ultra-low frequency with high energy conversion efficiency, Applied Energy, 279 (2020) 115762.

[11] N. Han, D. Zhao, J.U. Schluter, E.S. Goh, H. Zhao, X.J.A.E. Jin, Performance evaluation of 3D printed miniature electromagnetic energy harvesters driven by air flow, Applied Energy, 178 (2016) 672-680.

[12] Y. Li, Q. Cao, W. Zhang, Y. Zhang, J. a. Cao, A miniaturized electromagnetic energy harvester with volt-level output based on stacked flexible coils. Smart Materials and Structures, 27 (2018) 115040.

[13] L.-C. Zhao, H.-X. Zou, G. Yan, F.-R. Liu, T. Tan, K.-X. Wei, W.-M. Zhang, Magnetic coupling and flextensional amplification mechanisms for high-robustness ambient wind energy harvesting, Energy Conversion and Management, 201 (2019) 112166.

[14] Q. X. Tan, K. Q. Fan, K. Tao, L. Y. Zhao, M. L. Cai, A two-degree-of-freedom string-driven rotor for efficient energy harvesting from ultra-low frequency excitations, Energy, 196 (2020) 117107.

[15] Z.L. Wang, Piezoelectric nanogenerators based on zinc oxide nanowire arrays, Science, 312 (2006) 242-246.

[16] Z. Yang, L. Tang, K. Tao, K.C.J.S.M. Aw, A broadband electret-based vibrational energy

harvester using soft magneto-sensitive elastomer with asymmetrical frequency response profile, Smart Materials and Structures, 28 (2019) 10.

[17] S. Zhukov, H. von Seggern, X. Zhang, Y. Xue, O. Ben Dali, P. Pondrom, G. M. Sessler, M. Kupnik, Microenergy harvesters based on fluorinated ethylene propylene piezotubes, Advanced Engineering Materials, 22 (2020) 1901399.

[18] K. Tao, H. Yi, L. Tang, J. Wu, P. Wang, N. Wang, L. Hu, Y. Fu, J. Miao, H. Chang, Piezoelectric ZnO thin films for 2DOF MEMS vibrational energy harvesting, Surface and Coatings Technology, 359 (2019) 289-295 .

[19] K. Yang, J. Wang, D. Yurchenko, A double-beam piezo-magneto-elastic wind energy harvester for improving the galloping-based energy harvesting, Applied Physics Letters, 115 (2019) 193901.

[20] H. Liu, C.J. Tay, C. Quan, T. Kobayashi, C.K. Lee, Piezoelectric MEMS energy harvester for low-frequency vibrations with wideband operation range and steadily increased output power, J Microelectromech S, 20 (2011) 1131-1142.

[21] C.S. Wu, R.Y. Liu, J. Wang, Y.L. Zi, L. Lin, Z.L. Wang, A spring-based resonance coupling for hugely enhancing the performance of triboelectric nanogenerators for harvesting low-frequency vibration energy, Nano Energy, 32 (2017) 287-293.

[22] H. Zou, Y. Zhang, L. Guo, P. Wang, X. He, G. Dai, H. Zheng, C. Chen, A. C. Wang, C. Xu, Z.L. Wang, Quantifying the triboelectric series, Nature communications, 10 (2019) 1427.

[23] K.W. Han, J.N. Kim, A. Rajabi-Abhari, V.T. Bui, J.S. Kim, D. Choi, I.K. Oh, Long-lasting and steady triboelectric energy harvesting from low-frequency irregular motions using escapement mechanism, Adv Energy Mater, 11 (2020) 2002929.

[24] C. Li, D. Liu, C. Xu, Z. Wang, S. Shu, Z. Sun, W. Tang, Z.L. Wang, Sensing of joint and spinal bending or stretching via a retractable and wearable badge reel, Nature Communications, 12 (2021) 2950.

[25] X.H. Li, C.B. Han, T. Jiang, C. Zhang, Z.L. Wang, A ball-bearing structured triboelectric nanogenerator for nondestructive damage and rotating speed measurement, Nanotechnology, 27 (2016) 085401.

[26] Y. Jie, J. Ma, Y. Chen, X. Cao, N. Wang, Z.L. Wang, Efficient delivery of power generated by a rotating triboelectric nanogenerator by conjunction of wired and wireless transmissions using maxwell's displacement currents, Adv Energy Mater, 8 (2018) 1802084.

[27] X. Cheng, W. Tang, Y. Song, H. Chen, H. Zhang, and Z. L. Wang, Power management and effective energy storage of pulsed output from triboelectric nanogenerator, Nano Energy, 61(2019) 517-532.

[28] T. Ueno, Performance of improved magnetostrictive vibrational power generator, simple and high power output for practical applications, Journal of Applied Physics,

117 (2015) 17A740.

[29] H.J. Kim, J.H. Kim, K.W. Jun, J.H. Kim, W.C. Seung, O.H. Kwon, J.Y. Park, S.W. Kim, I.K.J.A.E.M. Oh, Silk nanofiber-networked bio-triboelectric generator, Adv Energy Mater, 6 (2016) 1502329.

[30] K. Tao, H.P. Yi, Y. Yang, H.L. Chang, J. Wu, L.H. Tang, Z.S. Yang, N. Wang, L.X. Hu, Y.Q. Fu, J.M. Miao, W.Z. Yuan, Origami-inspired electret-based triboelectric generator for biomechanical and ocean wave energy harvesting, Nano Energy, 67 (2020) 104-197.

[31] T. Huang, C. Wang, H. Yu, H. Wang, Q. Zhang, M. Zhu, Human walking-driven wearable all-fiber triboelectric nanogenerator containing electrospun polyvinylidene fluoride piezoelectric nanofibers, Nano Energy, 14 (2015) 226-235.

[32] V.T. Bui, J.H. Oh, J.N. Kim, Q. Zhou, I.K. Oh, Nest-inspired nanosponge-Cu woven mesh hybrid for ultrastable and high-power triboelectric nanogenerator, Nano Energy, 71 (2020) 104561.

[33] P. Wang, L. Pan, J. Wang, M. Xu, G. Dai, H. Zou, K. Dong, Z.L. Wang, An ultra-low-friction triboelectric-electromagnetic hybrid nanogenerator for rotation energy harvesting and self-powered wind speed sensor, ACS Nano, 12 (2018) 9433-9440.

[34] J. Wang, W. Ding, L. Pan, C. Wu, H. Yu, L. Yang, R. Liao, Z.L. Wang, Self-Powered wind sensor system for detecting wind speed and direction based on a triboelectric nanogenerator, ACS Nano, 12 (2018) 3954-3963.

[35] X. Chen, J. Xiong, K. Parida, M. Guo, P.S. Lee, Transparent and stretchable bimodal triboelectric nanogenerators with hierarchical micro-nanostructures for mechanical and water energy harvesting, Nano Energy, 64 (2019) 103904.

[36] W. Xu, H. Zheng, Y. Liu, X. Zhou, C. Zhang, Y. Song, X. Deng, M. Leung, Z. Yang, R.X. Xu, Z.L. Wang, X.C. Zeng, Z. Wang, A droplet-based electricity generator with high instantaneous power density, Nature, 578 (2020) 392-396.

[37] X. Cao, Y. Jie, N. Wang, Z.L. Wang, Triboelectric nanogenerators driven self-powered electrochemical processes for energy and environmental science, Adv Energy Mater, 6 (2016) 1600665.

[38] G. Liu, H. Guo, S. Xu, C. Hu, Z.L. Wang, Oblate spheroidal triboelectric nanogenerator for all-weather blue energy harvesting, Adv Energy Mater, (2019) 1900801.

[39] X. Zhao, G. Wei, X. Li, Y. Qin, D. Xu, W. Tang, H. Yin, X. Wei, L. Jia, Self-powered triboelectric nano vibration accelerometer based wireless sensor system for railway state health monitoring, Nano Energy, 34 (2017) 549-555.

[40] X.S. Zhang, M.D. Han, R.X. Wang, F.Y. Zhu, Z.H. Li, W. Wang, H.X. Zhang, Frequency-multiplication high-output triboelectric nanogenerator for sustainably powering biomedical microsystems, Nano Lett, 13 (2013) 1168-1172.

[41] S.Y. Kuang, J. Chen, X.B. Cheng, G. Zhu, Z.L. Wang, Two-dimensional rotary triboelectric nanogenerator as a portable and wearable power source for electronics,

Nano Energy, 17 (2015) 10-16.

[42] X. Cheng, B. Meng, X. Zhang, M. Han, Z. Su, H. Zhang, Wearable electrode-free triboelectric generator for harvesting biomechanical energy, Nano Energy, 12 (2015) 19-25.

[43] Y. Zou, A. Libanori, J. Xu, A. Nashalian, J. Chen, Triboelectric nanogenerator enabled smart shoes for wearable electricity generation, Research, 2020 (2020) 7158953.

[44] T. Zhou, C. Zhang, C.B. Han, F.R. Fan, W. Tang, Z.L. Wang, Woven structured triboelectric nanogenerator for wearable devices, ACS Appl Mater Interfaces, 6 (2014) 14695-14701.

[45] X. Qu, X. Ma, B. Shi, H. Li, L. Zheng, C. Wang, Z. Liu, Y. Fan, X. Chen, Z. Li, Z.L. Wang, Refreshable braille display system based on triboelectric nanogenerator and dielectric elastomer, Advanced Functional Materials, 31 (2020) 2006612.

[46] S. Wang, L. Lin, Z.L. Wang, Nanoscale triboelectric-effect-enabled energy conversion for sustainably powering portable electronics, Nano Letters, 12 (2012) 6339-6346.

[47] L. Lin, S. Wang, Y. Xie, Q. Jing, S. Niu, Y. Hu, Z.L. Wang, Segmentally structured disk triboelectric nanogenerator for harvesting rotational mechanical energy, Nano Lett, 13 (2013) 2916-2923.

[48] Y. Hu, J. Yang, Q. Jing, S. Niu, W. Wu, Z.L. Wang, Triboelectric nanogenerator built on suspended 3d spiral structure as vibration and positioning sensor and wave energy harvester, Acs Nano, 7 (2013) 10424-10432.

[49] Y. Yang, H. Zhang, J. Chen, Q. Jing, Y.S. Zhou, X. Wen, Z.L. Wang, Single-electrode-based sliding triboelectric nanogenerator for self-powered displacement vector sensor system, Acs Nano, 7 (2013) 7342-7351.

[50] S. Wang, Y. Xie, S. Niu, L. Lin, Z.L. Wang, Freestanding triboelectric-layer-based nanogenerators for harvesting energy from a moving object or human motion in contact and non-contact modes, Adv Mater, 26 (2014) 2818-2824.

[51] Z. Wu, S. Wang, Z. Cao, R. Ding, X.Y. Ye, Rotary disk multi-phase freestanding-electret generator with enhanced power and low ripple output, Nano Energy, 83 (2021) 105787.

[52] C.B. Han, W. Du, C. Zhang, W. Tang, L. Zhang, Z.L. Wang, Harvesting energy from automobile brake in contact and non-contact mode by conjunction of triboelectrication and electrostatic-induction processes, Nano Energy, 6 (2014) 59-65.

[53] M.Z. Bi, S.W. Wang, X.F. Wang, X.Y. Ye, Freestanding-electret rotary generator at an average conversion efficiency of 56%: Theoretical and experimental studies, Nano Energy, 41 (2017) 434-442.

[54] S. Niu, L. Ying, X. Chen, S. Wang, L.W. Zhong, Theory of freestanding triboelectric-layer-based nanogenerators, Nano Energy, 12 (2015) 760-774.

[55] Y. Xie, S. Wang, S. Niu, L. Lin, Q. Jing, Y. Su, Z. Wu, Z.L. Wang, Multi-layered disk

triboelectric nanogenerator for harvesting hydropower, Nano Energy, 6 (2014) 129-136.

[56] W. Tang, C. Zhang, C.B. Han, Z.L. Wang, Enhancing output power of cylindrical triboelectric nanogenerators by segmentation design and multilayer integration, Advanced Functional Materials, 24 (2014) 6684-6690.

[57] W. Li, Y. Pei, C. Zhang, A.G.P. Kottapalli, Bioinspired designs and biomimetic applications of triboelectric nanogenerators, Nano Energy, 84 (2021) 105865.

[58] S. Kim, Y. Suzuki, Photoelectric-charging-enhanced mems electret energy harvester with vacuum packaging, journal of physics conference, 773 (2016) 012012.

[59] K. Kittipaisalsilpa, T. Kato, Y. Suzuki, Characterization of fluorinated nematic liquid crystal for high-power electrostatic energy harvester, Journal of Physics Conference, 1052 (2018) 012044.

[60] X. Xia, J. Chen, H. Guo, G. Liu, D. Wei, Y. Xi, X. Wang, C. Hu, Embedding variable micro-capacitors in polydimethylsiloxane for enhancing output power of triboelectric nanogenerator, Nano Research, 10 (2016) 320-330.

[61] Y. Sakane, Y. Suzuki, N. Kasagi, The development of a high-performance perfluorinated polymer electret and its application to micro power generation, Journal of Micromechanics and Microengineering, 18 (2008) 104011.

[62] C. Han, Z. Chi, T. Wei, X. Li, L.W. Zhong, High power triboelectric nanogenerator based on printed circuit board (PCB) technology, Nano Research, 8 (2015) 722-730.

[63] K. Kashiwagi, K. Okano, T. Miyajima, Y. Sera, N. Tanabe, Y. Morizawa, Y. Suzuki, Microengineering, Nano-cluster-enhanced high-performance perfluoro-polymer electrets for energy harvesting, Journal of Micromechanics and Microengineering, 21 (2011) 125016.

[64] Y. Bai, L. Xu, S. Lin, J. Luo, H. Qin, K. Han, Z.L. Wang, Charge pumping strategy for rotation and sliding type triboelectric nanogenerators, Adv Energy Mater, 10 (2020) 2000605.

[65] W.C. Ko, C.K. Tseng, I.Y. Leu, W.J. Wu, S.Y. Lee, C.K. Lee, Use of 2-(6-mercaptohexyl) malonic acid to adjust the morphology and electret properties of cyclic olefin copolymer and its application to flexible loudspeakers, Smart Materials and Structures, 19 (2010) 55007-55015(9).

[66] B. Wang, Y. Chen, K. Tao, J. Wu, L. Tang, H. Chang, Enhanced Performance of a Rotary Energy Harvester with Bipolar Charged Electrets, 2018 IEEE/ASME Int. Conf. Adv. Intell. Mechatronics, IEEE, 2018, pp. 370-374.

[67] Z. Wu, M. Bi, Z. Cao, S. Wang, X. Ye, Largely enhanced electrostatic generator based on a bipolar electret charged by patterned contact micro-discharge and optimized substrates, Nano Energy, 71 (2020) 104602.

1